

Precursors to rock failure in the laboratory using ultrasonic monitoring methods

Veltmeijer, Aukje; Naderloo, Milad; Barnhoorn, Auke

DOI

[10.1007/s40948-024-00812-7](https://doi.org/10.1007/s40948-024-00812-7)

Publication date

2024

Document Version

Final published version

Published in

Geomechanics and Geophysics for Geo-Energy and Geo-Resources

Citation (APA)

Veltmeijer, A., Naderloo, M., & Barnhoorn, A. (2024). Precursors to rock failure in the laboratory using ultrasonic monitoring methods. *Geomechanics and Geophysics for Geo-Energy and Geo-Resources*, 10, Article 93. <https://doi.org/10.1007/s40948-024-00812-7>

Important note

To cite this publication, please use the final published version (if applicable). Please check the document version above.

Copyright

Other than for strictly personal use, it is not permitted to download, forward or distribute the text or part of it, without the consent of the author(s) and/or copyright holder(s), unless the work is under an open content license such as Creative Commons.

Takedown policy

Please contact us and provide details if you believe this document breaches copyrights. We will remove access to the work immediately and investigate your claim.



Precursors to rock failure in the laboratory using ultrasonic monitoring methods

Aukje Veltmeijer · Milad Naderloo ·
Auke Barnhoorn

Received: 16 November 2023 / Accepted: 7 May 2024
© The Author(s) 2024

Abstract Forecasting the occurrence of natural hazards, such as earthquakes or landslides, remain very challenging. These hazards are often caused by stress changes in the subsurface, therefore detecting and monitoring these changes can help the prediction and mitigation. Active ultrasonic transmission experiments were performed on Red Pfaelzer sandstones to investigate the monitoring and forecasting potential of these measurements. The sandstone samples were loaded until failure at different initial confining stress conditions. The forecasting potential to failure of different analysis methods, such as coda wave interferometry or wave attenuation, is investigated and compared. Our results show we can detect the forecast the upcoming failure of the samples from 40 to 70% of its failure point. Small differences between each analysis method are visible, but the trend of the signal is leading and therefore a robust prediction of failure can be made by combining analysis methods. In this paper, we propose a traffic light forecasting system using the precursory signals from ultrasonic monitoring. This

system is applicable for monitoring failure at various depths and or stress conditions, for a better prediction of small stress-induced changes in the subsurface and thus mitigation of failure (natural hazards) in the subsurface.

Article highlights

- Multiple waveform characteristics are compared for forecasting and monitoring potential of rock failure at different confining pressures.
- The upcoming failure of the rock samples can be forecasted from 40 to 70% of its failure point.
- A traffic light forecasting system using active acoustic monitoring is proposed to monitor and mitigate failure at various depths and or stress conditions.

Keywords Coda-wave decorrelation · Micro-fracture detection · Seismic attenuation · Rock failure

A. Veltmeijer (✉) · M. Naderloo · A. Barnhoorn
Geoscience and Engineering, Delft University
of Technology, Stevinweg 1, 2628 CN Delft,
The Netherlands
e-mail: a.v.veltmeijer@tudelft.nl

M. Naderloo
e-mail: m.naderloo@tudelft.nl

A. Barnhoorn
e-mail: auke.barnhoorn@tudelft.nl

1 Introduction

Natural hazards, such as earthquakes or landslides, can cause much damage. These events often result from precursory stress changes in the medium or along fault zones. Predicting the degree of these stress changes, and as a result, the potential onset and

exact location of failure or seismicity remain very challenging.

A lot of monitoring is done passively, e.g. recording seismic events after failure (Naderloo et al. 2023; Geller 1997). Hence, developing a robust method that can monitor these stress changes before failure is crucial for a better prediction and thus mitigation of failure and seismicity in the subsurface. To monitor the physical properties of the subsurface, remotely and non-destructively, geophysical methods can be used. Monitoring the seismic velocities provides insight into mechanical (rigidity, density, etc.) evolution (Schubnel et al. 2006). A number of geo-mechanical properties influence the propagation of elastic waves through a medium. Structural characteristics, including, rock type, mineralogy, porosity, and fluid type, but also environmental characteristics like effective stress (Hall 2009; Zhubayev et al. 2016; Barnhoorn et al. 2018; Sang et al. 2020), temperature (Snieder et al. 2002), and degree of saturation (Grêt et al. 2006b) change the elastic moduli and thus influence the wave propagation (Hall 2009). The stress changes can be quantified by analyzing the change in acoustic or seismic velocity (Xie et al. 2018; Sang et al. 2020). Stress changes in the subsurface can cause micro-crack formation (Cartwright-Taylor et al. 2022). This crack damage can lead to a decrease in elastic wave velocities (Barnhoorn et al. 2018; Sang et al. 2020), shear wave splitting (Peacock et al. 1988; Crampin and Chastin 2003), and in the development of anisotropy (Schubnel et al. 2006; Zhubayev et al. 2016). However, the sensitivity of seismic wave velocity to stress changes in rocks is low (Nur 1971; Grêt et al. 2006b, a; Barnhoorn et al. 2018) and detection of temporal variations is therefore difficult (Niu et al. 2003; Grêt et al. 2006a). By analyzing the direct arrivals, dispersion envelope, the coda wave or attenuation (Q-factor), stress changes in the subsurface can also be monitored (Snieder et al. 2006; Schubnel et al. 2006; Grêt et al. 2006b; Hall 2009; Zhubayev et al. 2016; Barnhoorn et al. 2018; Xie et al. 2018; Sang et al. 2020; Liu et al. 2022).

The coda wave can be used to monitor small changes in a medium, since it scatters throughout the rock and samples a disturbed region more than a direct wave (Snieder 2006). Therefore, small changes, like micro-crack damage, which may be undetectable in direct waves, are amplified by repeated sampling and detected by the coda. Coda waves are used in

many applications, such as monitoring of fault zones (Poupinet et al. 1984; Niu et al. 2008; Chiarabba et al. 2020b), volcanoes (Grêt et al. 2005; Snieder et al. 2006), the integrity of concrete (Deroo et al. 2010; Niederleithinger et al. 2018), temporal changes in the subsurface and in-situ stress (Grêt et al. 2006b, a), or to monitor velocity changes in laboratory experiments (Hadziioannou et al. 2009; Zotz-Wilson et al. 2019; Sang et al. 2020; Liu et al. 2022) and to locate these (Snieder and Vrijlandt 2005; Larose et al. 2010; Rossetto et al. 2011; Planès et al. 2015).

So far, laboratory studies on investigating changing rock properties have been unconfined uni-axial compressive strength experiments. Zotz-Wilson et al. (2019) and Liu et al. (2022) showed the use of coda wave interferometry to detect the yield point failure. Sang et al. (2020) did similar work, but also investigated S-waves and concluded that these showed higher sensitivity to structural changes in the rock samples. Barnhoorn et al. (2018), and Zhubayev et al. (2016) showed that attenuation factor Q can be used to describe the start of fracture formation in similar experiments. However, none of these studies have combined the various analysis methods to investigate the applicability of these properties under true subsurface conditions. In this study, we use S-waves to monitor the structural changes within the evolving medium in triaxial experiments to show both coda wave interferometry and attenuation properties can be used for monitoring and forecasting the failure of rock samples in the laboratory. We propose a traffic light forecasting system using the precursory signals from ultrasonic monitoring to monitor rock failure at various depths and or stress conditions and thus mitigation of failure (natural hazards) in the subsurface.

2 Methods

2.1 Experimental procedure

Shear wave propagation is influenced by changes in density and elastic moduli caused by structural changes due to deformation. We show different applications of ultrasonic transmission measurements to monitor the structural changes within a Red Pfaelzer sandstone sample. These sandstones are used as an analog for Groningen reservoir rock and the properties of the individual sample are listed in Table 1. The

Table 1 Summary of the Red Pfaelzer samples, confining pressure P_c , porosity ϕ , length L, diameter D, and Young’s Modulus E, which is calculated from the stress–strain relationship

Sample	P_c (MPa)	ϕ (%)	L (mm)	D (mm)	E (GPa)
RF610	0	23.35	60.30	29.75	8.60
RF613	2.5	23.48	60.25	29.65	9.79
RF28	5	23.44	60.60	29.65	10.83
RF23	10	24.94	61.70	29.65	12.44
RF68	20	23.82	61.65	29.65	15.94
RF614	20	22.72	60.40	29.55	13.39
RF69	40	22.20	60.35	29.70	13.74
RF615	40	23.25	60.55	29.75	13.44
AL ref	10 & 20	0	60	30	75

All samples were water-saturated

porosity was determined to be between 22 and 25%, using a gas expansion (Helium) pycnometer. The samples have a fairly homogeneous composition of 89% quartz, 6% orthoclase (Eradus 2019) (Fig. 1h–k). Used are cylindrical core samples with a diameter of 30 ± 0.5 mm and 60 ± 2 mm length, such that the length/diameter ratio is 1:2. A total of 8 uni-axially

deformation experiments are performed at different confining pressures ranging from 2.5 to 40 MPa and one UCS experiment (or 0 MPa confining pressure) (Fig. 1a–g). Simultaneously to the loading of the rock, ultrasonic transmission measurements are done. This combined setup enables us to measure the wave properties under changing stress conditions.

The triaxial experiments were conducted using a Hoek-cel (Fig. 2) which was placed in a homemade uniaxial loading frame with a 500 kN loadcell. Confining pressure was maintained using an ISCO pump model 100DM. The experiments are performed on vacuum-saturated samples at room temperature. First, the samples are hydrostatically brought up to the confining pressure in steps of 1 MPa. After reaching the desired confining pressure, it is then set constant for the entire experiment. The samples are deformed at a constant strain rate of 0.005 s^{-1} . The shortening of the sample is recorded with two Solartron AX/1/S linear variable displacement transducers (LVDT’s) and is corrected for machine deformation. The axial stress was measured using a load cell positioned above the sample (Fig. 2).

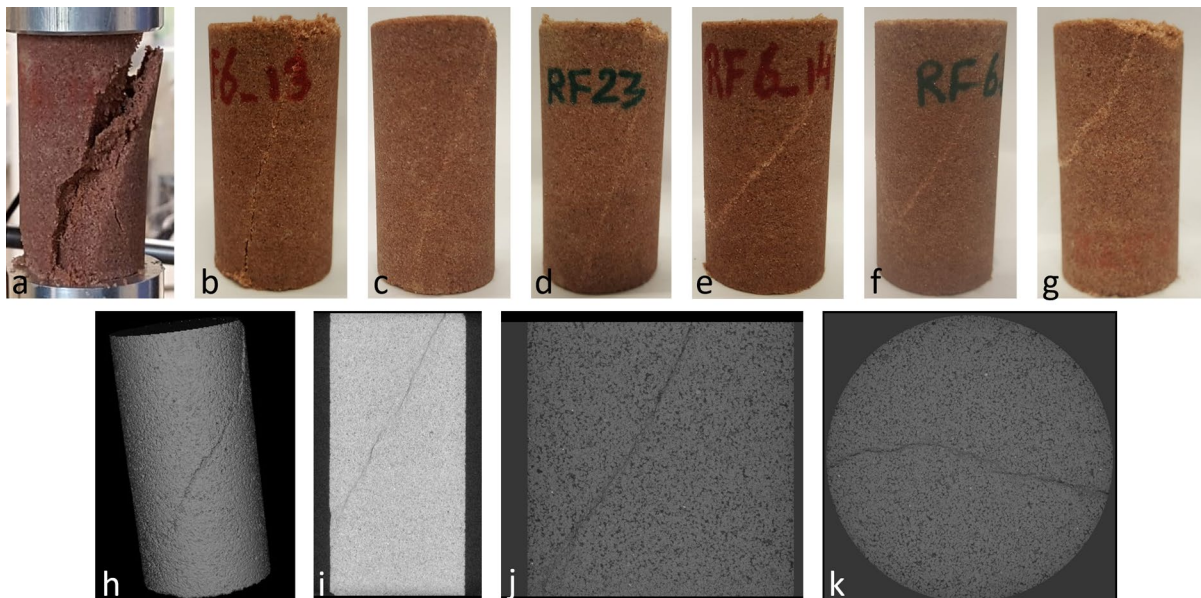
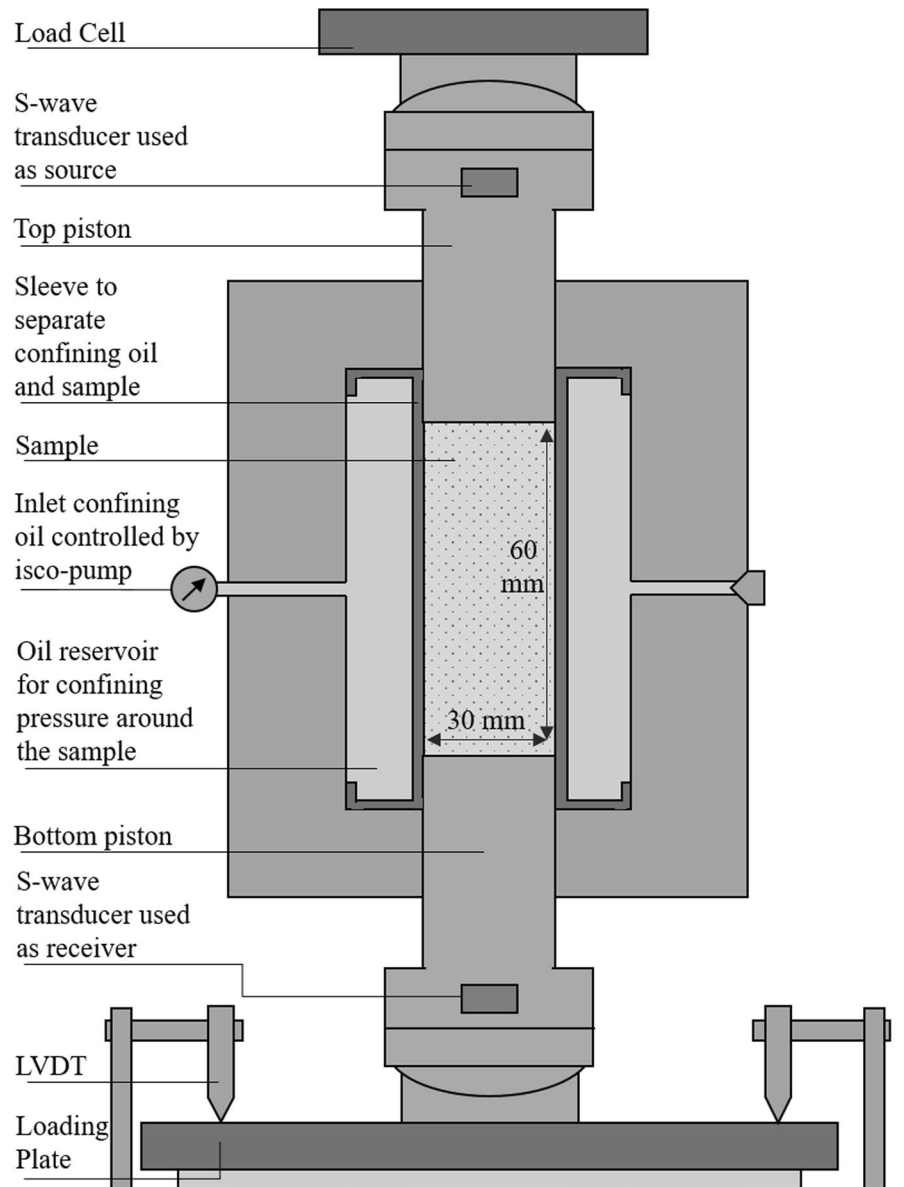


Fig. 1 Pictures of the fractured rock samples in a–g, from left to right fractured with 0–40 MPa confining pressure. In a sample RF610, b sample RF613, c RF28, d RF23, e RF14, f sample RF68, g sample RF69. CT images of sample RF614 in h–k made by CoreTOM microCT scanner in h a volume rep-

resentation of the sample with a resolution of $73.7 \mu\text{m}$ and in i YZ slice with a resolution of $73.7 \mu\text{m}$. j, k show a higher resolution zoom on the fracture and the grains in the sample with a resolution of $12.2 \mu\text{m}$. In j a YZ slice, and in k a XY slice

Fig. 2 Schematic illustration of instrumented Hoek cell with S-wave transducers integrated into the pistons (not to scale). The shortening of the sample was recorded with two linear variable displacement transducers (LVDT's), which record the total (vertical) movement of the loading plate. The axial stress was measured using a load cell



The ultrasonic transmission measurements are performed using two S-wave transducers, with a peak operating frequency of 1 MHz. An Agilent 33210A waveform generator generated the waveforms which were amplified by an RF Power amplifier, sent and received using Olympus 1 MHz/.5" v153 transducers, and finally recorded using a Yokogawa DL9240L oscilloscope. The two axial transducers are integrated into the pistons in the loading system with a source

at the top and receiver at the bottom, such that the polarization of the shear source and receiver transducers was always aligned. The ultrasonic transmission signals are recorded every 10 s for 100 μ s and are a stack of 256 (S-) waves to increase the signal-to-noise ratio. The ultrasonic transmission monitoring started immediately after starting the deformation and continued during the whole duration of the deformation experiment.

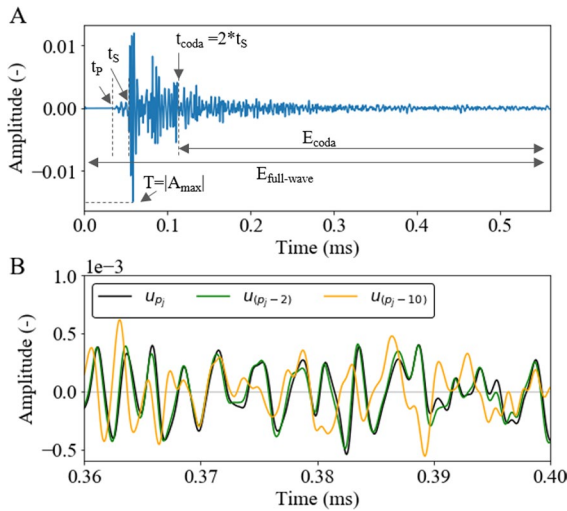


Fig. 3 Showing recorded transmission wavelets. **A** showing the arrival times of P-wave (t_p), S-wave (t_s), and the start of the coda (t_{coda}). The range used for the energy calculation is indicated for the energy of the total- and coda wave as well as the maximum amplitude for the transmissivity. **B** shows a part of the coda of three wavelets. Where u_{p_j} is the to-be correlated wavefield and is lagging behind the reference wavefield by $N = 2$ and $N = 10$

2.2 Data analysis

To monitor the onset and development of fracturing within the rock the coda wave and the attenuation of the recorded waves are investigated. The coda wave is used to monitor the change in scattering properties, while the Q-factor, energy, and transmissivity are all a proxy of attenuation. Coda Wave Interferometry (CWI) is used to monitor the velocity change between two recorded waves. Comparing the consecutive wavefields is done with a cross-correlation (CC) (Fig. 3), for a time window of width $2t_w$ and centered around time t_k , and reaches its maximum if the travel time perturbation δt across all possible perturbed paths P is $\delta t = t_s$. Assuming the time shift is constant in the considered time window, the relative velocity change (dv/v) can be written as $\delta v/v = -\delta t/t$.

In addition to the velocity change, the decorrelation coefficient is determined to investigate the changes in material scattering (Planès et al. 2014, 2015). The method of Coda Wave Decorrelation (CWD) introduced by Larose et al. (2010) is based on the theory of Snieder (2006). The decorrelation

coefficient K between the perturbed (u_p) and unperturbed wavefield (u_u), also described in Zotz-Wilson et al. (2019), is formulated as

$$K(t_s) = 1 - CC(t_s) = 1 - \frac{\int_{t_k-t_w}^{t_k+t_w} u_{p_j-N}(t)u_{p_j}(t+t_s)dt}{\sqrt{\int_{t_k-t_w}^{t_k+t_w} u_{p_j-N}^2(t)dt \int_{t_k-t_w}^{t_k+t_w} u_{p_j}^2(t)dt}} \tag{1}$$

To monitor the changing medium, a moving reference wavefield $u_{(p_j-N)}(t)$ is used, where N is the number of measurements the reference wavefield is lagging behind the to-be correlated wavefield $u_{p_j}(t)$ (Fig. 3B). While the coda waves seem random due to the complex paths they take through the medium, the changes they are subjected to are strongly related to the position and strength of the changes in the medium (Planès et al. 2014). K is related to the changes in material scattering due to the addition of scatterers (Planès et al. 2014, 2015), such as the addition or removal of fractures. The scattering in a medium along the transport mean free path l can be described using the cross-sectional area of a single scatterer σ and the density of scatterers ρ (Planès et al. 2014). The total scattering coefficient as described by Aki and Chouet (1975) is given by $g_0 = \rho\sigma = l^{-1}$. Following the theory in Aki and Chouet (1975), we can rewrite the coda decorrelation in terms of the scattering coefficient (g_0) between a perturbed (p) and unperturbed (u) medium (Zotz-Wilson 2020).

$$K(t) = \frac{v_0}{2} t |\Delta g_{0_{p-u}}|, \tag{2}$$

where $K(t)$ is the theoretical decorrelation coefficient, t the time in the coda and v_0 the velocity in the medium. Using a shifting reference, the changes in the absolute value of $|g_0|$ are monitored as a rate of change (Zotz-Wilson 2020). In these deformation experiments, the change in scattering is mostly attributed to the closure or formation and growth of microfractures. Closure of pre-existing pore space (such as microfractures) and compaction of the medium cause a reduction in the scattering cross-sectional area and thus a reduction in K . During compaction and closure of pre-existing pore space, the attenuation is expected to decrease, and energy and transmissivity to increase. The formation of microfractures, leading to failure, results in an increase in the total scattering cross-section σ and the number density of scatterers

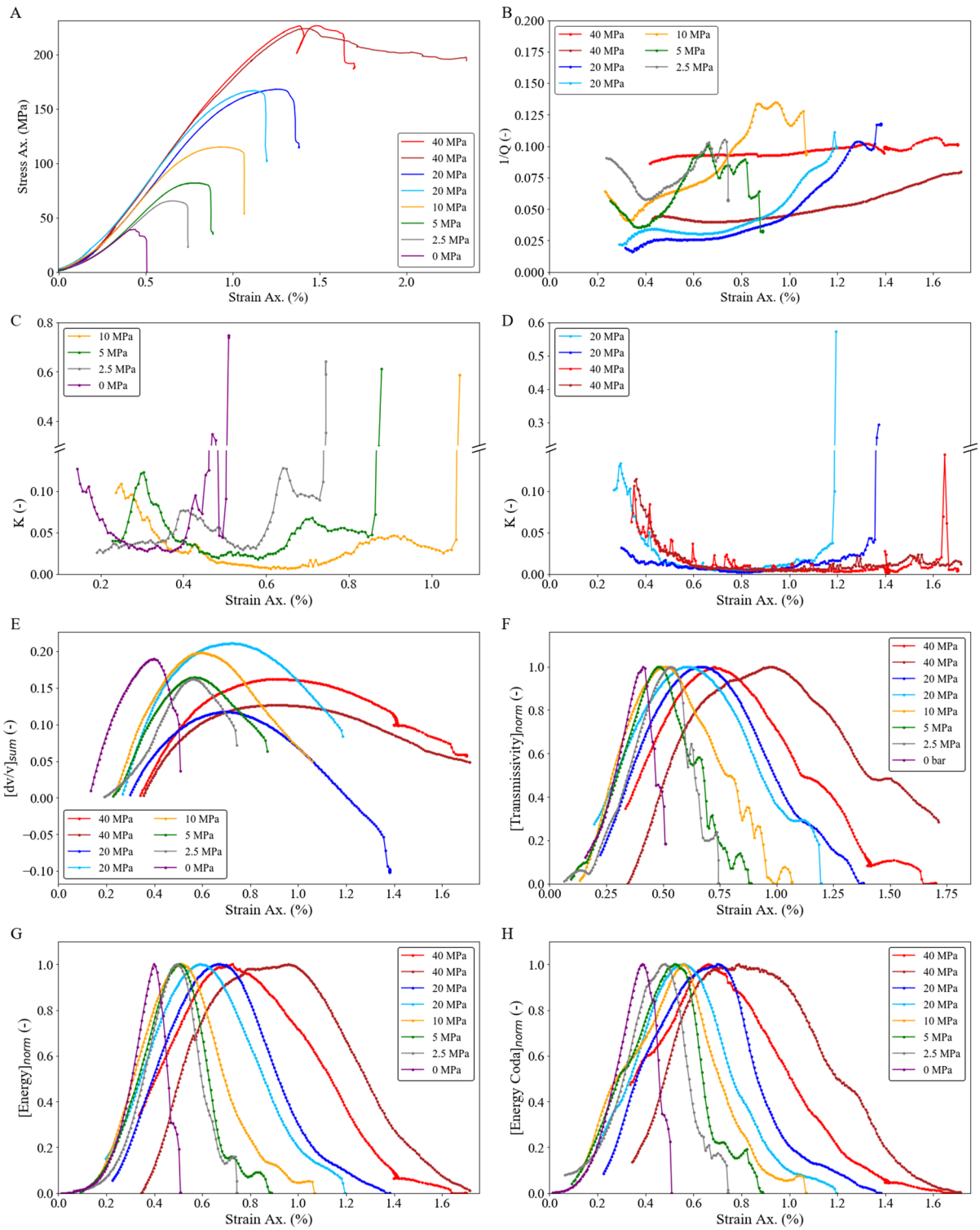


Fig. 4 The stress–strain, and seismic parameters during deformation experiment for all confining pressures. **A** showing the stress–strain relations. **B** showing the evolution of the attenuation $1/Q$ during deformation. **C**, **D** show the evolution of the decorrelation coefficient K for the lower and higher confining pressures. **E** shows the cumulative velocity change $[dv/v]_{sum}$. **F** shows the evolution of the transmissivity T , normalized to the maximum of each experiment for better comparison. **G**, **H** show the energy of the full wave E_T and energy of the coda E_C , respectively. The values of each are normalized to their max for better comparison

ρ , both contributing to an increase of the total scattering coefficient.

The formation and growth of micro-fractures increase the attenuation and cause the waves to lose energy and increased arrival time. The ultrasonic attenuation is determined using the laboratory method by Toksoz et al. (1979) also described in Zhubayev et al. (2016) and Barnhoorn et al. (2018) by comparing the rock sample to an aluminium reference. Assuming a constant Q , the spectral ratio is written as

$$\ln \frac{A_1}{A_2} = (\beta_2 - \beta_1)xf + \ln \frac{G_1}{G_2}, \quad (3)$$

where A_i is the Fourier amplitude, f is the frequency, x is the propagation distance and G_i is a scaling factor for spherical spreading independent of frequency. $i = 1$ refers to the aluminium reference and 2 to the rock sample. β_i is related to the quality factor by

$$Q_i = \frac{\pi}{\beta_i V}, \quad (4)$$

where V is the P- or S- velocity. β_1 is very small compared to β_2 , due to the very low attenuation of the aluminium and is henceforth ignored. The energy of waves can be a good method for crack monitoring (Michaels et al. 2005; Mi et al. 2006) and is approximated as $E(\sigma) = \int_{t_2}^{t_1} u^2(t;\sigma)dt$, where $u(t;\sigma)$ is the recorded waveform (Michaels et al. 2005; Mi et al. 2006; Sagar 2009; Khazaei et al. 2015). The transmitted wave amplitudes are defined as $T = |A_{max}|$ (Shreedharan et al. 2021), which is the maximum amplitude of the recorded S-wave (Fig. 3A).

3 Results

The deformation of rock samples in the laboratory is commonly characterized into 5 stages: crack closure, the elastic stage, stable crack growth, unstable cracking, and rock failure (Bieniawski 1967; Eberhardt et al. 1999; Zhou et al. 2018). The stress–strain curves obtained by triaxial testing at the defined confining pressures (Fig. 4A) show a non-linear increase at low stresses caused by the initial setting of the machine, elastic compaction of the rock, and closure of existing pore space e.g. the closure of micro-cracks pre-existing in the sample (Walsh 1965; Bieniawski 1967; Eberhardt et al. 1999; Zhou et al. 2018). This is followed by an elastic (reversible) deformation stage, where a linear stiffening of the rock matrix is expected, visible as a linear gradient in the stress–strain curves. After the elastic stage, the stress–strain curve shows non-linear behaviour, indicating the formation of the first micro-fractures (Barnhoorn et al. 2010). The crack formation continues until the stresses drop drastically, indicating the failure of the sample. Increasing the confining pressure leads to an expected increase in the maximum strength and Young’s modulus of the sample.

During the deformation of the sample, ultrasonic transmission measurements were performed (Fig. 5). Coda wave decorrelation (CWD) was used to monitor structural and velocity changes in the medium, following the results of Zotz-Wilson et al. (2019). K shows an average of 10 independent correlation windows, with the first starting at twice the S-arrival time ($t_{coda} = 2 * t_S$) (Fehler et al. 1992; Pujades et al. 1997), in total the coda windows span 0.84 ms. Using a shifting reference, the decorrelation coefficient K is a measure of change in the absolute value of $|g_0|$, therefore, a decreasing trend indicates a reduction in the scattering of the waveform compared to its previous. A reduction is visible at the start of the experiments for each tested confining pressure (Fig. 4C, D). This reduction is followed by a plateau of limited change in K , with thereafter an increase indicating an increasing scattering coefficient, during the deformation stage of formation and growth of (micro-) fractures.

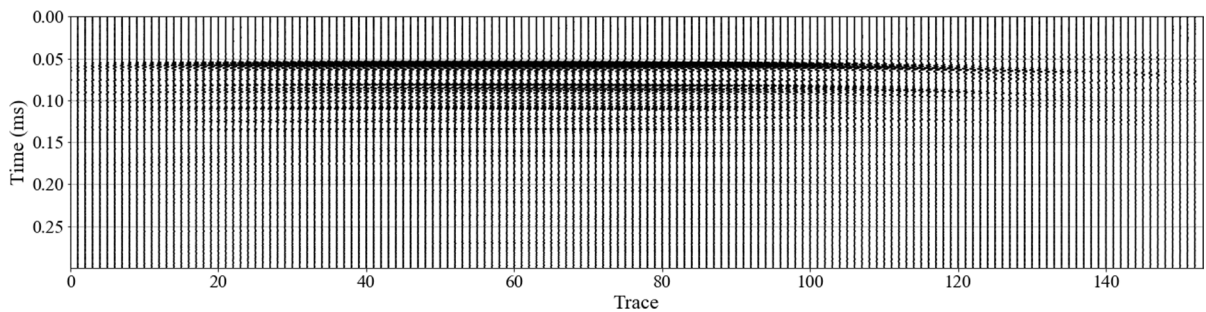


Fig. 5 First 0.25 ms of all the recorded S-waves during the uni-axial 10 MPa confining pressure compression experiment. The waveforms are recorded every 10 s and are a stack of 256 S-waves

Additionally to K, the velocity change during the experiment was determined using coda wave interferometry (CWI). The CWI, using a shifting reference, gives the rate of change in velocity, by cumulative summation of the average relative velocity change, the velocity change during the experiment is obtained (Fig. 4E). This shows a parabolic trend indicating the compaction and formation and growth of (micro-) fractures during the experiments. Similar parabolic trends can be seen in the energy and transmissivity data (Fig. 4F–H), where the initial increase can be explained by the compaction of the rock matrix and the following decrease by the formation of micro-fractures (Shah and Hirose 2010; Zotz-Wilson et al. 2019; Zotz-Wilson 2020). Additional to the energy and transmissivity, the evolution of the ultrasonic attenuation (Fig. 4B) and frequency content of the waveforms provide insight into the deformation of the sandstones.

The energy of waves can be attenuated by fractures in the rock sample. Changes in the ultrasonic transmission waveforms are detected when the attenuation effects due to fracture formation are larger than the compaction and shortening effects due to loading. During loading, the samples are subjected to a constant strain rate. This results in shortening and compaction and causes a shorter direct travel path, as well as a faster path, due to increased velocity, for the transmitted waves. Together with the closure of pre-existing pore-space in the rock matrix these result in an increase in energy, transmissivity, and relative velocity (Fig. 4E–H). The fractures induced by this continued deformation reverse this effect, decreasing the velocity of the matrix and increasing attenuation causing the waves to lose energy and arrive at an increased arrival

time. The competition between these factors results in the parabolic trends of transmissivity, velocity change, and energy. The peak of these parabolas, the change from an increasing to decreasing trend, is around the point the gradient of the stress–strain curve changes to non-linearity and shows the first indication of (micro-) fracture formation and growth. Within these parabolic trends, a more complex pattern in the S-wave amplitudes emerges around the peak stress, for the lower confining pressures. This pattern is also visible in the evolution of the Q-factor (attenuation) (Fig. 4B), which is inversely related to the energy and transmissivity of the S-waves. The frequency content of the recorded wave changed during the experiment (Fig. 7D, I). The normalized amplitude spectra of the frequency show a shift towards the lower frequencies, due to the increased presence of micro-fractures. Upon failure the high frequencies are mostly attenuated and the lower persevere.

4 Discussion

4.1 Ultrasonic monitoring and forecasting failure

The first sign of permanent deformation, namely the formation of (micro-) fractures resulting ultimately in the failure of the sample, is the change to non-linearity in the gradient of the stress–strain relation. However, this stress–strain relation is impossible to determine in-situ (i.e. landslides, earthquakes, etc.). To detect deformation without stress and/or strain measurements, we focused on the change in seismic response throughout deformation, using the advantage that active source methods do not rely on acoustic emission to detect any deformation, and thus can

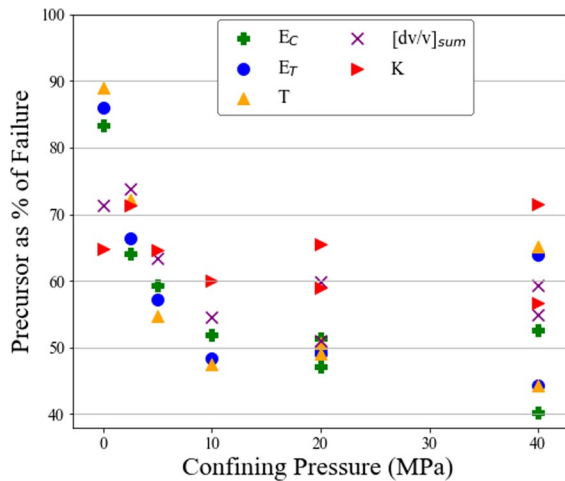


Fig. 6 Appearance of the peak in the energy of the full wave E_T and coda wave E_C , the cumulative velocity change $[dv/v]_{sum}$, and the transmissivity T, as well as the minimum of the decorrelation coefficient K as precursor relative to the failure of the sample

be used to monitor both aseismic and seismic deformation. The attenuation and scattering properties of the waves change due to the formation and growth of the (micro-) fractures in the samples.

Precursors to failure were determined from these waveform attributes. The evolution of the energy E, relative velocity change dv/v , and transmissivity T show a clear change in slope as the fractures formed are detected (Fig. 4E–H). The decorrelation coefficient K shows an increase in scattering when the fractures are formed and detected by the coda (Fig. 4C, D). Therefore, the minimum before this increasing trend in the K, and the peaks of E, dv/v , and T are used as the earliest precursor to the imminent failure of the sample. The occurrence of these precursors is plotted relative to the failure of the sample, where at 100% failure occurs according to the stress–strain relation (Fig. 6). For the uniaxial compressive strength (UCS) experiments, the precursors obtained from coda wave decorrelation (CWD) are significantly earlier than the precursors based on attenuation properties. They range from 65 to 72% for K and dv/v and between 84 and 88% for the attenuation parameters E, dv/v , and T. This changes with increasing confining pressure, where the precursors based on attenuation are generally earlier. Which of the precursors to failure is the first varies and comes as early as 40% of failure for 40 MPa confining pressure. At higher

confining pressures, the precursors are relatively earlier but also show a bigger spread.

To forecast the upcoming failure of the sample, we deployed a traffic light warning system (TLS) based on the interpretation of the processed waveform data and the occurrence of the precursors (Fig. 7).

1. According to our traffic light, it is green or safe when our sample is far from its failure. The closure of pre-existing pore space, stiffening, and compaction of the rock is indicated by a decrease in scattering K, and an increase in the E, T, and $[dv/v]_{sum}$.
2. The orange stage can be classified as a stage of higher alert in which failure of the sample is expected, and be used to forecast the upcoming failure. This stage starts at the first occurrence of precursors of the waveform attributes. In Fig. 7, E, dv/v , and T change to a decreasing trend indicating the attenuation effect due to newly formed (micro-) fractures is stronger than the continued compaction and shortening of the sample. This is at around 50% of the final failure point of the sample (Fig. 6).
3. The last stage represents that failure is imminent. The warning stage starts when K shows an increase in scattering, giving a clear indication (micro-) fractures are formed. A clear indication of fracture formation and thus upcoming failure is present when the energies, transmissivity, and relative velocity change show a decreasing trend and the decorrelation coefficient starts to increase. Additionally, the frequency content of the recorded wave shifts towards the lower frequencies as the higher frequencies are attenuated, due to the increased formation and growth of (micro-) fractures.

From experiment to experiment, the first precursor varies (Fig. 6), but for monitoring and forecasting purposes, not one precursory signal is superior over the other. By combining the various analysis techniques on a single wavelet, the impact of the sensitivity of a single parameter is limited and a more robust TLS forecast can be made. Even though precursory signals vary for confining pressure, the results show that the trend in the processed data of the S-waves is very similar for all tested confining pressures. It is, therefore, suggested that

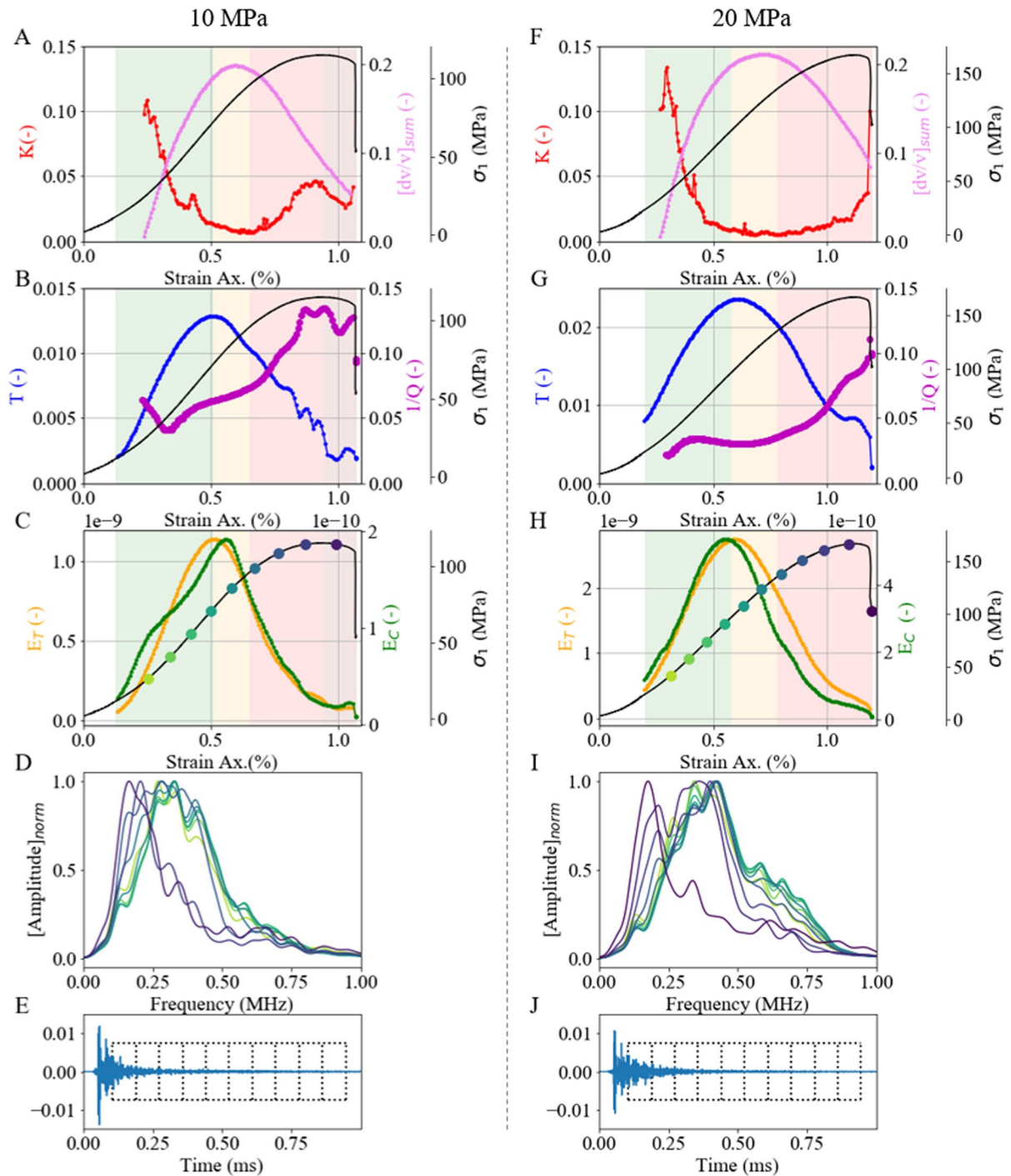


Fig. 7 Precursory signals during the deformation in **A–E** at 10 and in **F–J** at 20 MPa confining pressure. Showing the cumulative velocity change from CWI dv/v_{sum} and decorrelation coefficient K in **A, F**, the attenuation $1/Q$ and transmissivity T in **B, G**, and the energy of the full wave E_T and coda wave E_C in **C, H** together with the stress–strain relation. **D, I** showing the changing frequency content of the recorded waves

during deformation. **D, I** show the stage of deformation of the frequency content plotted, corresponding to the colours of the dots in **C, H**. **E, J** show a recorded waveform during deformation, the 10 decorrelation windows are visualized, with the first starting at 2 times the S-arrival time ($t_{coda} = 2 * t_s$), and a total length of 0.84 ms. The coloured zones in **A–C** and **F–H** show the three stages of the traffic light warning system (TLS)

these techniques could be deployed for monitoring the failure of rocks, at any depth or pressure condition. Monitoring is possible at any arbitrary point in time or stress condition, using a shifting reference, and by using the traffic light system, the frequency of measurements can be increased near failure to obtain an even more accurate forecast.

The precursors we showed in this paper, could be used to forecast at approximately 70% of the failure point. In a laboratory setting, this might be seconds or minutes, at the field scale, this could be hours, days or longer, which can provide time for mitigation measures. The application and scalability of ultrasonic monitoring from laboratory to field scale will have to be researched. However, research has shown precursory signals could be measured at a field scale. Niu et al. (2008), showed stress-induced changes in crack properties during co-seismic slip using active source cross-well experiment at the San Andreas Fault or Chiarabba et al. (2020a), showed a local P-wave velocity reduction near the hypocentre for a few weeks before the mainshock using seismic tomography at the fault zone which participated in the 2016 M6.5 Norcia earthquake, Italy.

4.2 Effect of pressure

The competition between the attenuation and scattering effect of fracture formation and compaction and shortening of the sample results in a clear precursory signal for all tested confining pressures. The difference between confining pressures tested, for our purpose of monitoring and forecasting failure, is of lesser importance but gives us some more insight into the process of deformation and sensitivity of the used S-waves in the detection of micro-fractures.

4.2.1 Deformation rate

The experiments are all performed with a loading rate of 0.005 s^{-1} , at high confining pressure, larger stresses are needed to achieve failure of the sample. As a result, these rock samples have a lengthier elastic stage and a slower fracture formation. Due to the (relative) slower deformation at high pressure, relatively more waveforms are recorded per deformation stage. Consequently, less change in the scattering in the medium from waveform to reference waveform is detected.

This also implies that, at higher confining pressures, the deformation is better monitored than at low confining pressures, as a constant sampling rate of 10 s was used. Therefore, the deformation at 40 MPa confining pressure was sampled best. During the deformation, K shows several sharp peaks showing rapid, but short changes in the sample (Fig. 4D). From the nature of the shifting reference, these peaks can be interpreted as the change from the signal before. Crack formation increases the amount of scattering, thus K. If, at the sampling time, no new crack is formed, no additional scattering is created, thus K goes down again. Hence, we interpret these peaks at the start of the experiment as the sharp closure of larger or a couple of pre-existing fractures present in the rock sample. During a later stage of deformation, these peaks indicate the formation of micro-cracks, large enough to be sampled by the ultrasonic waves and frequency used. When deformation is fast, crack formation follows each other in quick succession, resulting in an increase in scattering and K, without individual crack formation visible. This implies that for slow deformation and a high sampling rate, the separate crack formation can be monitored, contingent on wave sensitivity.

This relative deformation speed is also clearly visible in the velocity change during deformation, when plotted cumulative to represent the absolute velocity change the graphs differ from pressure to pressure, however when we plot the derivative, the rate of the velocity change decreases with confining pressure, showing a slower rate of deformation at higher pressure (Fig. 8).

4.2.2 Deformation around peak strength

The difference in deformation due to confining pressure is also visible in the maxima of the waveform attributes (Fig. 9), At higher pressures fractures form with small or closed apertures causing less additional scattering and attenuation opposed to open tensile fractures. The maximum value of K obtained during the failure of the sample shows a decreasing trend with increasing pressure. Opposite, the maximum energy and transmissivity measured increase with confining pressure. The source wavelet for all experiments remained constant, due to increased compaction more of the initial wave energy is preserved at higher initial confining stresses. A reduced scattering

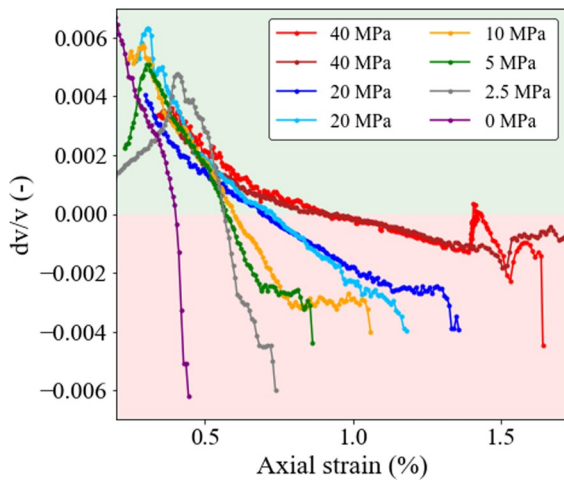


Fig. 8 The rate of velocity change dv/v during deformation for each confining pressure tested. Showing the relative deformation rate changes with confining pressure

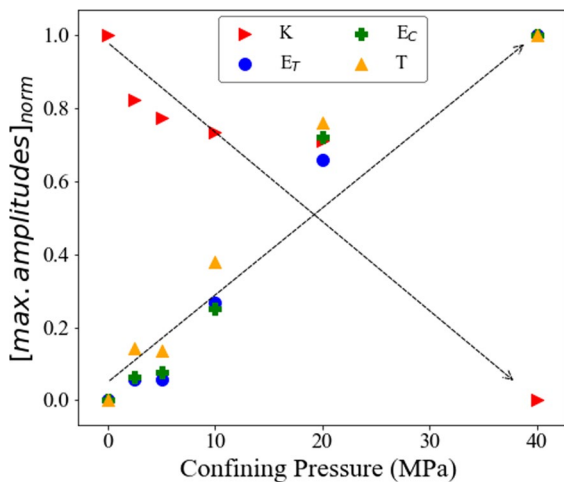


Fig. 9 The maximum value recorded for each precursor. Showing decreasing trend with pressure in decorrelation coefficient K , and an increasing trend in the energy of the full wave E_T and coda wave E_C , and transmissivity T

effect of the shear compared to tensile fractures results in decreasing values of K . This implies that tensile fractures or fractures with a bigger aperture are better detected, due to the higher scattering nature of the tensile fracture.

Near the failure point of the stressed rock samples, the formed micro-fractures start to connect and form larger-scale shear fractures. At lower confining

pressures, a more complex pattern in the transmissivity emerges around the peak stress (Fig. 4B, F–H). The attenuation (Q -factor), energy, and transmissivity for the lower confining pressures oscillate. We suggest this oscillating behaviour observed in our data, is the detection of the connecting shear fractures near failure. The transmissivity and energy increase due to the continued shortening and compaction of the sample. The moment the fractures are formed and connected into larger ones, the attenuation increases, and the energies and transmissivity drop. While the sample is not failing yet and is still shortened and compacted, the formed fractures (partially) close and the attenuation decreases until the next local failure forms the next larger fracture, resulting in the observed oscillations. This oscillation is only visible when the sample shows less brittle behaviour, when the sample collapses at or very close to peak strength this oscillation is not observed suggesting all the micro-fractures connect rapidly in one large shear fracture. At higher confining pressure the potential to form fractures with aperture is very small, therefore we state that this oscillation is not present due to the lack of sensitivity of the waves and less brittle behaviour of the samples at higher pressures.

5 Conclusion

In projects such as underground storage of gas or CO_2 or geothermal energy, especially near densely populated areas, there is an increased need for robust monitoring system for a safe use of the subsurface. Our experimental results demonstrate the monitoring potential of active seismic measurements and offer a traffic light system to safely manage the subsurface.

Ultrasonic experiments have been conducted on Red Pfaelzer sandstones (analog to the Groningen reservoir rock) to investigate the potential of shear wave transmission measurements in monitoring the upcoming failure. Ultrasonic monitoring can monitor the changes in the subsurface, while passive acoustic emission methods could be late in detecting the upcoming failure. Our results show the failure of the tested samples can be forecasted from 40 to 70% of the failure point. A robust prediction can be made by combining the various analysis techniques, without having to do multiple measurements. Which precursor to failure first varies, and comes as early as 40% of

failure at high pressure, but for forecasting purposes, not one precursory signal is superior over the other.

In this study, the stress–strain relations were available, therefore the small details in the waveforms could be explained by relating the signals to the deformation stages of the stress–strain relation. The precursors show small differences between tested confining pressures, but as the trends are very similar, we argue that the proposed traffic light monitoring system is applicable for forecasting failure at various depths and or stress conditions. Monitoring can be started at any arbitrary point in time or stress condition using a shifting reference. For field measurements, additional research and feasibility studies will have to be performed, but the shown monitoring methods in this paper can be applicable in field situations when stress–strain measurements are not possible. Contributing to a robust monitoring technique that can detect small stress-induced changes in the subsurface and use these for a better prediction and thus mitigation of failure (and seismicity) in the subsurface.

Acknowledgements We would like to thank the laboratory support staff at TUDelft, specifically Marc Friebe and Karel Heller for their guidance in the lab.

Author contributions AV: Conceptualization, methodology, experiments, visualization, writing original draft, and editing; MN: methodology, writing: review and editing, experiments; AB: conceptualization, supervision, grant acquiring, writing: review and editing.

Funding This research was funded by NWO Science domain (NWO-ENW), Project DEEP.NL.2018.048.

Data availability The laboratory facilities at TU Delft were used to perform the experiments and record the data (loading data and waveforms) used in this publication. This data is accessible at the 4TU.ResearchData repository under a CC BY 4.0 licence. <https://doi.org/10.4121/21557910> (Veltmeijer et al. 2023).

Declarations

Conflict of interest The authors declare no conflict of interest.

Ethics approval Not applicable.

Consent for publication All authors have seen the manuscript and approved to submit to the journal.

Open Access This article is licensed under a Creative Commons Attribution 4.0 International License, which permits use, sharing, adaptation, distribution and reproduction in any medium or format, as long as you give appropriate credit to the original author(s) and the source, provide a link to the Creative Commons licence, and indicate if changes were made. The images or other third party material in this article are included in the article's Creative Commons licence, unless indicated otherwise in a credit line to the material. If material is not included in the article's Creative Commons licence and your intended use is not permitted by statutory regulation or exceeds the permitted use, you will need to obtain permission directly from the copyright holder. To view a copy of this licence, visit <http://creativecommons.org/licenses/by/4.0/>.

References

- Aki K, Chouet B (1975) Origin of coda waves: source, attenuation, and scattering effects. *J Geophys Res* 80(23):3322–3342. <https://doi.org/10.1029/jb080i023p03322>
- Barnhoorn A, Cox SF, Robinson DJ, Senden T (2010) Stress- and fluid-driven failure during fracture array growth: implications for coupled deformation and fluid flow in the crust. *Geology* 38(9):779–782. <https://doi.org/10.1130/G31010.1>
- Barnhoorn A, Verheij J, Frehner M, Zhubayev A, Houben M (2018) Experimental identification of the transition from elasticity to inelasticity from ultrasonic attenuation analyses. *Geophysics* 83(4):MR221–MR229. <https://doi.org/10.1190/geo2017-0534.1>
- Bieniawski ZT (1967) Mechanism of brittle fracture of rock. Part I-theory of the fracture process. *Int J Rock Mech Min Sci*. [https://doi.org/10.1016/0148-9062\(67\)90030-7](https://doi.org/10.1016/0148-9062(67)90030-7)
- Cartwright-Taylor A, Mangriotis MD, Main IG, Butler IB, Fusesis F, Ling M, Magdysyuk OV (2022) Seismic events miss important kinematically governed grain scale mechanisms during shear failure of porous rock. *Nat Commun*. <https://doi.org/10.1038/s41467-022-33855-z>
- Chiarabba C, De Gori P, Segou M, Cattaneo M (2020) Seismic velocity precursors to the 2016 Mw 6.5 Norcia (Italy) earthquake. *Geology* 48(9):924–928. <https://doi.org/10.1130/G47048.1>
- Chiarabba C, De Gori P, Segou M, Cattaneo M (2020) Seismic velocity precursors to the 2016 Mw 6.5 Norcia (Italy) earthquake. *Geology* 48(9):924–928. <https://doi.org/10.1130/G47048.1>
- Crampin S, Chastin S (2003) A review of shear wave splitting in the crack-critical crust. *Geophys J Int* 155(1):221–240. <https://doi.org/10.1046/j.1365-246X.2003.02037.x>
- Deroo F, Kim J-Y, Qu J, Sabra K, Jacobs LJ (2010) Detection of damage in concrete using diffuse ultrasound. *J Acoust Soc Am* 127(6):3315–3318. <https://doi.org/10.1121/1.3409480>
- Eberhardt E, Stead D, Stimpson B (1999) Quantifying progressive pre-peak brittle fracture damage in rock

- during uniaxial compression. *Int J Rock Mech Min Sci* 36(3):361–380. [https://doi.org/10.1016/S0148-9062\(99\)00019-4](https://doi.org/10.1016/S0148-9062(99)00019-4)
- Eradus D (2019) Petrographical description and petrophysical measurements on the Red Felser sandstone (B.Sc. Thesis). Delft University of Technology
- Fehler M, Hoshiba M, Sato H, Obara K (1992) Separation of scattering and intrinsic attenuation for the Kanto-Tokai region, Japan, using measurements of S-wave energy versus hypocentral distance. *Geophys J Int* 108(3):787–800. <https://doi.org/10.1111/j.1365-246X.1992.tb03470.x>
- Grêet A, Snieder R, Aster RC, Kyle PR (2005) Monitoring rapid temporal change in a volcano with coda wave interferometry. *Geophys Res Lett* 32(6):1–4. <https://doi.org/10.1029/2004GL021143>
- Geller RJ (1997) Earthquake prediction: a critical review. *Geophys J Int* 131(3):425–450. <https://doi.org/10.1111/j.1365-246x.1997.tb06588.x>
- Grêet A, Snieder R, özbay U (2006) Monitoring in situ stress changes in a mining environment with coda wave interferometry. *Geophys J Int* 167(2):504–508. <https://doi.org/10.1111/j.1365-246X.2006.03097.x>
- Grêet A, Snieder R, Scales J (2006) Time-lapse monitoring of rock properties with coda wave interferometry. *J Geophys Res Solid Earth* 111(3):1–11. <https://doi.org/10.1029/2004JB003354>
- Hadziioannou C, Larose E, Coutant O, Roux P, Campillo M (2009) Stability of monitoring weak changes in multiply scattering media with ambient noise correlation: laboratory experiments. *J Acoust Soc Am* 125(6):3688–3695. <https://doi.org/10.1121/1.3125345>. [arXiv:0904.3384](https://arxiv.org/abs/0904.3384)
- Hall SA (2009) When geophysics met geomechanics: imaging of geomechanical properties and processes using elastic waves. In: Kolymbas, D., Viggiani, G. (eds.) Chapter VIII. Springer
- Khazaei C, Hazzard J, Chalaturnyk R (2015) Damage quantification of intact rocks using acoustic emission energies recorded during uniaxial compression test and discrete element modeling. *Comput Geotech* 67:94–102. <https://doi.org/10.1016/j.compgeo.2015.02.012>
- Larose E, Planès T, Rossetto V, Margerin L (2010) Locating a small change in a multiple scattering environment. *Appl Phys Lett* 96(20):1–4. <https://doi.org/10.1063/1.3431269>
- Liu S, Ma B, Ma Z, Sun J, Wang Q, Liu K (2021) Evaluation of the compressional damage evolution of ancient fired clay bricks using coda wave analysis. *J Build Eng* 49:104071. <https://doi.org/10.1016/j.jobte.2022.104071>
- Mi B, Michaels JE, Michaels TE (2006) An ultrasonic method for dynamic monitoring of fatigue crack initiation and growth. *J Acoust Soc Am* 119(1):74–85. <https://doi.org/10.1121/1.2139647>
- Michaels JE, Michaels TE, Mi B, Cobb AC, Stobbe DM (2005) Self-calibrating ultrasonic methods for in-situ monitoring of fatigue crack progression. *AIP Conf Proc* 760(2005):1765–1772. <https://doi.org/10.1063/1.1916884>
- Naderloo M, Veltmeijer A, Jansen JD, Barnhoorn A (2023) Laboratory study on the effect of stress cycling pattern and rate on seismicity evolution. *Geomech Geophys Geo-Energy Geo-Resour* 9(1):1–18. <https://doi.org/10.1007/s40948-023-00678-1>
- Niederleithinger E, Wang X, Herbrand M, Müller M (2018) Processing ultrasonic data by coda wave interferometry to monitor load tests of concrete beams. *Sensors* (Switzerland). <https://doi.org/10.3390/s18061971>
- Niu F, Silver PG, Nadeau RM, McEvilly TV (2003) Migration of seismic scatterers associated with the 1993 Parkfield aseismic transient event. *Nature* 426(6966):544–548. <https://doi.org/10.1038/nature02151>
- Niu F, Silver PG, Daley TM, Cheng X, Majer EL (2008) Pre-seismic velocity changes observed from active source monitoring at the Parkfield SAFOD drill site. *Nature* 454(7201):204–208. <https://doi.org/10.1038/nature07111>
- Nur A (1971) Effects of stress on velocity anisotropy in rocks with cracks. *J Geophys Res* 76(8):2022–2034. <https://doi.org/10.1029/jb076i008p02022>
- Peacock S, Crampin S, Booth DC, Fletcher JB (1988) Shear wave splitting in the Anza Seismic Gap, southern California: temporal Variations as possible precursors. *J Geophys Res Solid Earth* 93(B4):3339–3356. <https://doi.org/10.1029/JB093iB04p03339>
- Planès T, Larose E, Margerin L, Rossetto V, Sens-Schönfelder C (2014) Decorrelation and phase-shift of coda waves induced by local changes: multiple scattering approach and numerical validation. *Waves Random Complex Media* 24(2):99–125. <https://doi.org/10.1080/17455030.2014.880821>
- Planès T, Larose E, Rossetto V, Margerin L (2015) Imaging multiple local changes in heterogeneous media with diffuse waves. *J Acoust Soc Am* 137(2):660–667. <https://doi.org/10.1121/1.4906824>
- Poupinet G, Ellsworth WL, Frechet J (1984) Monitoring velocity variations in the crust using earthquake doublets: an application to the Calaveras fault, California (USA). *J Geophys Res* 89(B7):5719–5731. <https://doi.org/10.1029/JB089iB07p05719>
- Pujades L, Ugalde A, Canas JA, Navarro M, Badal FJ, Corchete V (1997) Intrinsic and scattering attenuation from observed seismic codas in the Almería Basin (southeastern Iberian Peninsula). *Geophys J Int* 129:281–291. <https://doi.org/10.1016/j.pepi.2004.02.004>
- Rossetto V, Margerin L, Planès T, Larose É (2011) Locating a weak change using diffuse waves: theoretical approach and inversion procedure. *J Appl Phys* 10(1063/1):3544503
- Sagar RV (2009) An experimental study on acoustic emission energy and fracture energy of concrete. In: Proceedings of the national seminar and exhibition on non-destructive evaluation, pp 225–228
- Sang G, Liu S, Elsworth D (2020) Quantifying fatigue-damage and failure-precursors using ultrasonic coda wave interferometry. *Int J Rock Mech Min Sci* 131(February):104366. <https://doi.org/10.1016/j.ijrmms.2020.104366>
- Schubnel A, Benson PM, Thompson BD, Hazzard JF, Paul Young R (2006) Quantifying damage, saturation and anisotropy in cracked rocks by inverting elastic wave velocities. *Pure Appl Geophys* 163:947–973. <https://doi.org/10.1007/s00024-006-0061-y>
- Shah AA, Hirose S (2010) Nonlinear ultrasonic investigation of concrete damaged under uniaxial compression step loading. *J Mater Civ Eng* 22(5):476–484. [https://doi.org/10.1061/\(asce\)mt.1943-5533.0000050](https://doi.org/10.1061/(asce)mt.1943-5533.0000050)

- Shreedharan S, Bolton DC, Rivière J, Marone C (2021) Competition between preslip and deviatoric stress modulates precursors for laboratory earthquakes. *Earth Planet Sci Lett* 553:116623. <https://doi.org/10.1016/j.epsl.2020.116623>
- Snieder R (2006) The theory of coda wave interferometry. *Pure Appl Geophys* 163(2–3):455–473. <https://doi.org/10.1007/s00024-005-0026-6>
- Snieder R, Vrijlandt M (2005) Constraining the source separation with coda wave interferometry: theory and application to earthquake doublets in the Hayward fault, California. *J Geophys Res Solid Earth* 110(4):1–15. <https://doi.org/10.1029/2004JB003317>
- Snieder R, Grêet A, Douma H, Scales J (2002) Coda wave interferometry for estimating nonlinear behavior in seismic velocity. *Science* 295(5563):2253–2255. <https://doi.org/10.1126/science.1070015>
- Snieder R, Prejean SG, Johnson JB (2006) Spatial variation in Mount St. Helens clones from coda wave analysis. *Centre Wave Phenom Consort Project* 2006:247–252
- Toksoz MN, Johnston DH, Timur A (1979) Attenuation of seismic waves in dry and saturated rocks -I. Laboratory measurements. *Geophysics* 44(4):681–690. <https://doi.org/10.1190/1.1440970>
- Veltmeijer A, Naderloo M, Barnhoorn A (2023) Supporting data for the article “forecasting of rock failure in the laboratory using active acoustic monitoring methods” [dataset]. 4TU.ResearchData. <https://data.4tu.nl/datasets/f3785220-65f0-4e13-8659-5cd1d258ed63>
- Walsh JB (1965) The effect of cracks on the compressibility of rock. *J Geophys Res* 70(2):381–389. <https://doi.org/10.1029/JZ070i002p00381>
- Xie F, Ren Y, Zhou Y, Larose E, Baillet L (2018) Monitoring local changes in granite rock under biaxial test: a spatiotemporal imaging application with diffuse waves. *J Geophys Res Solid Earth* 123(3):2214–2227. <https://doi.org/10.1002/2017JB014940>
- Zhou S, Xia C, Zhou Y (2018) A theoretical approach to quantify the effect of random cracks on rock deformation in uniaxial compression. *J Geophys Eng* 15(3):627–637. <https://doi.org/10.1088/1742-2140/aaa1ad>
- Zhubayev A, Houben ME, Smeulders DM, Barnhoorn A (2016) Ultrasonic velocity and attenuation anisotropy of shales, Whitby, United Kingdom. *Geophysics* 81(1):D45–D56. <https://doi.org/10.1190/GEO2015-0211.1>
- Zotz-Wilson R (2020) Coda-wave monitoring of continuously evolving material properties. Ph.D. dissertation, Delft University of Technology. <https://doi.org/10.4233/uuid:9c0b2f03-040b-4ec8-b669-951c5acf1f3b>
- Zotz-Wilson R, Boerrigter T, Barnhoorn A (2019) Coda-wave monitoring of continuously evolving material properties and the precursory detection of yielding. *J Acoust Soc Am* 145(2):1060–1068. <https://doi.org/10.1121/1.5091012>. [arXiv:1808.02732](https://arxiv.org/abs/1808.02732)

Publisher's Note Springer Nature remains neutral with regard to jurisdictional claims in published maps and institutional affiliations.